

**RESEARCH ARTICLE** OPEN ACCESS

# Characterization of Nitinol Produced by Laser Powder Bed Fusion for Mechanical Metamaterial Applications

 Ondřej Červinek<sup>1</sup>  | Jakub Hurník<sup>1</sup> | Miroslav Šmíd<sup>2</sup> | Ondřej Zobač<sup>2</sup> | Melanie Todt<sup>3</sup> | Daniel Koutný<sup>1</sup>
<sup>1</sup>Institute of Machine and Industrial Design, Brno University of Technology, Brno, Czech Republic | <sup>2</sup>Institute of Physics of Materials, Czech Academy of Sciences, Brno, Czech Republic | <sup>3</sup>Institute of Lightweight Design and Structural Biomechanics, Technical University of Vienna, Vienna, Austria

**Correspondence:** Ondřej Červinek ([160793@vutbr.cz](mailto:160793@vutbr.cz))

**Received:** 24 September 2025 | **Revised:** 26 January 2026 | **Accepted:** 17 February 2026

**Keywords:** cyclic loading | differential scanning calorimetry | laser powder bed fusion | nitinol | superelasticity

## ABSTRACT

This study investigates the relationship between the process parameters of the laser powder bed fusion technology and the functional properties of nitinol metamaterial for morphing actuator applications. Using an extraordinary wide range of laser powers (40–400 W) and scanning speeds (175–3000 mm s<sup>-1</sup>) provides the most comprehensive assessment of resulting morphologies, allowing identification of defect-free configurations, especially for low energy densities. The assessment is done with respect to porosity, thin-wall dimensional accuracy, crystallography, austenite–martensite phase transformation, and recoverability under cyclic loading. The results show that low volumetric energy density of 41–55 J mm<sup>-3</sup> can lead to an internal porosity of less than 0.1%, although brittle cracking may occur. The cyclic compression tests show a variable quasilinear pseudoelasticity with low hysteresis. The highest total strain after 50 cycles is 5.43% with an associated cumulative residual strain of 2.79%, stabilizing after approximately 30 cycles. The recoverable strain decreases with increasing load, most significantly from 53.4% at 800 MPa to 35.1% at 1200 MPa. The computational estimation of metamaterial morphing capability provides reliable results if the linear assumption after the fifth cycle is adopted by the material model and geometrical thickness deviations are reflected.

## 1 | Introduction

Nickel–titanium alloys have become of great interest for high-end biomedical and aerospace applications because of their unique ability to undergo large deformations (to 8~10%) and return to their original, undeformed shape [1, 2]. Such behavior can fully exploit its potential in thin-walled elements, such as mechanical metamaterials embedded in medical stents or morphing wing actuators, where complex mechanisms can be replaced with one highly flexible component. Recoverability is achieved either by the application of heat—shape memory effect (SME) or by the release of stress—superelastic effect (SE). The SME/SE are enabled by a reversible phase transformation between the austenitic phase B2 (*A*) and the martensitic phase B19' (*M*) [3, 4].

To use nitinol metamaterial in morphing actuator applications, such as leading and trailing edges of aircraft wings or flexible

components in payload separation systems, a high-fidelity parent material must be provided first [5]. Such material has to allow for a large actuation range in a relatively stiff metamaterial component without cracking, defect evolution, or progressive degradation of recoverability, which until recently was considered impossible [6, 7]. However, the unprecedented design and processing freedom brought by laser powder bed fusion (L-PBF) have enabled tailoring of nitinol capabilities that leverage both the material's intrinsic properties and architectural design principles to achieve tailored mechanical responses [8]. Unfortunately, the extreme thermal gradients, rapid solidification rates (10<sup>3</sup>–10<sup>6</sup> K/s), and repeated thermal cycling inherent to L-PBF processing fundamentally alter microstructural evolution, compositional homogeneity, and phase transformation behavior [9, 10]. For thin-walled metamaterials, where feature sizes can drop below 0.2 mm, and thermal histories vary dramatically with wall

This is an open access article under the terms of the [Creative Commons Attribution](https://creativecommons.org/licenses/by/4.0/) License, which permits use, distribution and reproduction in any medium, provided the original work is properly cited.

© 2026 The Author(s). *Advanced Engineering Materials* published by Wiley-VCH GmbH.

thickness and local geometry, these effects become particularly pronounced and poorly understood.

Previous research has shown that the sensitivity of thermomechanical response to process parameters, even when different parameter combinations led to the same energy density [11, 12]. This compositional sensitivity becomes critically important in L-PBF processing, where selective evaporation of the more volatile nickel constituent can occur from the melt pool [12]. As a consequence, the transformation temperatures and functional properties exhibited extreme swings, with shifts of approximately 10°C per 0.1 at.% change in nickel content near the equiatomic composition. Additionally, the precipitation of secondary phases, particularly Ni<sub>4</sub>Ti<sub>3</sub> in Ni-rich compositions and Ti<sub>2</sub>Ni in Ti-rich compositions, profoundly affects transformation behavior by depleting the matrix of nickel or titanium, respectively. This finding challenges the conventional energy density framework and suggests that melt pool dynamics, particularly peak temperatures and residence times above the nickel boiling point, govern compositional evolution more directly than integrated energy input. Multiple investigations have established that optimal volume energy density (VED) should not exceed 90 J mm<sup>-3</sup> for achieving high relative density (>98–99%) while minimizing defects [13, 14] to prevent increased nickel loss, impurity pickup, and excessive crack formation. Alternative metrics have been proposed by Gustmann et al., who used line energy  $E_L$  to optimize thin lattice struts, achieving fully melted struts at  $E_L > 150 \text{ J m}^{-1}$  with diameters of 130–170 μm. The more sophisticated approach was presented by Timercan et al. [15], who utilized a coupled VED build rate framework that identified optimal conditions within build rate 3–10 cm<sup>3</sup> h<sup>-1</sup> at VED not exceeding 90 J mm<sup>-3</sup>. In contrary, Ge et al. [16] restricted successful specimens printing with VED not exceeding 75.8 J mm<sup>-3</sup>.

Load history is another important factor to consider when developing metamaterials for actuators, as recoverability decreases with the number of load cycles [11, 17]. The recoverability degradation of nitinol is driven by progressive dislocation accumulation that stabilizes martensite and suppresses transformation, microcrack nucleation and growth at defects or stress concentrations, precipitate coarsening or redistribution that alters transformation behavior and residual stress evolution. According to Saedi et al., the superelastic behavior of nitinol specimens fabricated by L-PBF can be stabilized after the 10<sup>th</sup> cycle [18]. In contrast, Henderson et al. identified stabilization up to the 40<sup>th</sup> cycle [19]. Related to metamaterials, Chen et al. found that nitinol gradient lattice structures achieved a recoverable displacement rate of at least 99.15% after six cycles [20]. This results in performance inconsistency in bulk specimens and nitinol metamaterials made by L-PBF. As possible reasons, different scan speed or hatch distance resulting in variable energy density [21], microstructural factors, precipitates, composition, or heat treatment of tested specimens can be identified. Further investigation of cyclic tensile loading with increasing loads and stress-controlled fatigue showed that the higher proportion of retained martensite reduces fatigue life [22]. In addition, an increase in residual strain and a decrease in elastic modulus can be observed when the maximum compressive strain increases under cyclic loading [23].

The functional properties of L-PBF nitinol lattices exhibit strong dependencies on geometric parameters, including strut

diameter, unit cell size, porosity, and architectural topology, although the mechanisms underlying these geometric effects remain subjects of active investigation. Iasnii et al. [24] have shown that the termination temperature of austenitic transformation in bulk nitinol rods is much lower compared to that of thin struts in lattice structures. In addition, the L-PBF fabrication of thin-walled nitinol parts has shown favorable results in achieving higher geometric accuracy with lower scanning speeds, especially in the case of parts with small struts (0.2–0.6 mm) [25]. Gustmann et al. [26] revealed extreme sensitivity of strut diameter to scan vector length, with 0.01 mm vectors producing  $150 \pm 9 \mu\text{m}$  struts compared to  $222 \pm 10 \mu\text{m}$  for 0.1 mm vectors at identical energy inputs. This geometric sensitivity suggests that thermal accumulation and heat-affected zone interactions become dominant factors at small length scales, necessitating adaptive scanning strategies rather than simple parameter scaling from bulk processing conditions. The coupling between wall thickness and scanning speed presents a particular complexity. Guo et al. [27] investigated this interaction in thin-wall structures, finding that transformation temperature deviation among different wall thicknesses increased from ~3.7°C at 400 mm s<sup>-1</sup> scanning speed to ~23.5°C at 600 mm s<sup>-1</sup>. In addition, the surface quality of a build is significantly influenced by the scanning speed to laser power ratio [10]. Ratio values greater than 0.3 or lower than 0.1 result in a considerable number of spherical pores [28].

Efficient development of metamaterial actuators requires pushing nitinol processability to the level of complex geometries with an understanding of L-PBF phenomenological behavior induced by process parameters [29, 30]. This behavior can be interpreted using material and geometry characteristics determined for a specific thin-walled production setup [31]. While material behavior was widely discussed in previous years [29, 30], the geometry of thin-walled nitinol elements got far less attention. Yet it is the geometry that can significantly impact the exploitation capabilities of the material superelasticity potential [32, 33]. The research gap in geometrical perspective can be identified in the coupled effects of manufacturing deviations and thermal history, which vary for different L-PBF production conditions and therefore complicate individual design efficiency estimation in finite element analysis (FEA) [34]. In addition, cyclic stability and functional fatigue behavior of metamaterials have been described by limited sources, suggesting potential concerns regarding permanent strain accumulation [35]. It restricts the achievable superelastic morphing capabilities in thin-walled metamaterials and hinders the scalability of laboratory-tested processing conditions to larger and more complex components. Most studies examine bulk specimens or small coupons, leaving unclear whether the identified processing windows and property relationships transfer to components with complex geometry, varying stress–strain distribution, and complex thermal management challenges. Based on the literature [30, 36], a broad window of process parameters was defined and further investigated with respect to morphological, mechanical, and geometrical aspects to identify configurations best suited for metamaterial morphing actuators. The study provides an experimentally sound, production-specific description of nitinol behavior oriented to thin-walled elements. In addition, forms a solid basis for the development of metamaterial actuators, taking full advantage of the superelasticity potential.

## 2 | Materials and Methods

The following section describes the main analyses carried out from the single-track inspection towards the assessments of morphing metamaterial transformation limits.

### 2.1 | Powder Characteristics

The gas-atomized nitinol metal powder (Carpenter Additive, Widnes, United Kingdom) was selected for the manufacturing of the specimen. The shape of the particles was analyzed using a scanning electron microscope (SEM, Table 1, Figure 1). The particle size distribution was determined by laser size diffraction using the ASTM B822 standard. The powder tap density was determined to be  $4.26 \text{ kg m}^{-3}$  using the ASTM B527 standard. The chemical powder composition of the nitinol alloy is given in Table 2.

### 2.2 | Production of Nitinol Specimens

The specimen production was carried out using an SLM 280HL machine (SLM Solutions Group AG, Lübeck, Germany). A ytterbium Gaussian-mode fiber laser YLR-400-WC-Y11 (IPG Photonics, Oxford, USA) with 400 W maximum power, a spot diameter of  $82 \mu\text{m}$ , and a wavelength of  $1070 \text{ nm}$  was used. A reduced  $100 \times 100 \text{ mm}$  nitinol base plate and a standard silicone recoater blade were used to produce specimens. Tables 3 and 4 give the machine setup and process parameters window used.

TABLE 1 | Size distribution of nitinol powder.

Quantile	$Q_{10}$	$Q_{50}$	$Q_{90}$
Particle size, $\mu\text{m}$	13.3	30	51.2

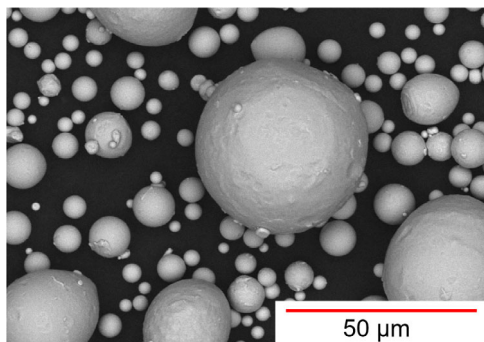


FIGURE 1 | Nitinol powder morphology. SEM image.

TABLE 2 | Chemical composition of nitinol powder.

Elem. <sup>a</sup>	Ni	C	Cr	Co	Cu	H	Fe	Nb	N	O	Ti
wt.%	55.75	0.0024	0.0042	$<10^{-3}$	$<0.0035$	$<0.0005$	0.0044	$<10^{-3}$	$<0.0005$	0.058	Bal.

<sup>a</sup>Data from the powder supplier.

TABLE 3 | Machine setup for the production process.

Parameter	Layer thickness $L$ , $\mu\text{m}$	Platform heating, $^{\circ}\text{C}$	Atmosphere, -	Residual oxygen content, %
Value	50	200	Ar	$<0.2$

The parameter selection was based on the range of line energies described in [30, 36] but intentionally extended to test limits leading to track discontinuity induced by the lack of fusion effect in one extreme, and keyholing sourced from surplus of energy in the other extreme. The line energy was calculated using the following expression [37]:

$$E_L = \frac{P}{V} [J \cdot \text{mm}] \quad (1)$$

where  $P$  is the laser power and  $V$  denotes the laser speed.

Table 5 shows the types and geometric parameters of the test specimens selected from a narrow range after evaluation of a single-track experiment. The primary aim of this study is to investigate thin-walled elements, but the minimal allowed volume tested for the intended analyses exceeds that available for thin-walled elements. Furthermore, results must be determined as a representative value independent of the influence of surface and subsurface regions. For this purpose, some of the following analyses were performed on cylindrical specimens. In addition, three different configurations of metamaterial segments were produced (Figure 2), two of which were designed with a slight auxetic behavior. Geometries frequently used in other studies for conventionally produced materials were intentionally chosen to demonstrate superelastic morphing capabilities [38, 39].

### 2.3 | Microscope Image Analysis

The Keyence VHX-2500 digital microscope (Keyence, Osaka, Japan) with the Z250R objective ( $\times 250$  zoom) was used to obtain detailed information on the cross-sectional geometry and porosity of the specimens. The microscope images of the specimen cross-sections were analyzed using the JavaScript-based open-source plugin ImageJ2 Fiji (National Institutes of Health, Bethesda, Maryland, USA). The images were converted to grayscale with a range of 0–255 (0-white, 255-black) to detect pores and borders. Then, the threshold filter was applied to select a range of 110–255. In the next step, the images were transferred to binary maps in which the porosity and dimensions of the specimens were recognized based on binary criteria.

### 2.4 | Transformation Temperatures

The transformation temperatures of the nitinol produced by L-PBF were determined using differential scanning calorimetry (DSC). For this purpose, specimens with dimensions  $4 \times 4 \times 1 \text{ mm}$  [3] were cut from the cylinders using the electrical discharge

TABLE 4 | The L-PBF process parameters to produce single tracks.

Parameter	Scanning speed V, mm s <sup>-1</sup>	Laser Power P, W	E <sub>L</sub> , J·m <sup>-1</sup>
1	175	40	229
2	250	40	160
3	500	40	80
4	750	40	53
5	175	80	457
6	250	80	320
7	500	80	160
8	750	80	107
9	1000	80	80
10	1250	80	64
11	1500	80	53
12	1750	80	46
13	175	120	686
14	250	120	480
15	500	120	240
16	750	120	160
17	1000	120	120
18	1250	120	96
19	1500	120	80
20	1750	120	69
21	2000	120	60
22	2500	120	48
23	175	160	914
24	250	160	640
25	500	160	320
26	750	160	213
27	1000	160	160
28	1250	160	128
29	1500	160	107
30	1750	160	91
31	2000	160	80
32	2500	160	64
33	3000	160	53
34	250	200	800
35	500	200	400
36	750	200	267
37	1000	200	200
38	1250	200	160
39	1500	200	133
40	1750	200	114
41	2000	200	100
42	2500	200	80
43	3000	200	67
44	250	240	960

(Continues)

TABLE 4 | (Continued)

Parameter	Scanning speed V, mm s <sup>-1</sup>	Laser Power P, W	E <sub>L</sub> , J·m <sup>-1</sup>
45	500	240	480
46	750	240	320
47	1000	240	240
48	1250	240	192
49	1500	240	160
50	1750	240	137
51	2000	240	120
52	2500	240	96
53	3000	240	80
54	250	280	1120
55	500	280	560
56	750	280	373
57	1000	280	280
58	1250	280	224
59	1500	280	187
60	1750	280	160
61	2000	280	140
62	2500	280	112
63	3000	280	93
64	500	320	640
65	750	320	427
66	1000	320	320
67	1250	320	256
68	1500	320	213
69	1750	320	183
70	2000	320	160
71	2500	320	128
72	3000	320	107
73	500	360	720
74	750	360	480
75	1000	360	360
76	1250	360	288
77	1500	360	240
78	1750	360	206
79	2000	360	180
80	2500	360	144
81	3000	360	120
82	500	400	800
83	750	400	533
84	1000	400	400
85	1250	400	320
86	1500	400	267
87	1750	400	229
88	2000	400	200

(Continues)

TABLE 4 | (Continued)

Parameter	Scanning speed V, mm s <sup>-1</sup>	Laser Power P, W	E <sub>L</sub> , J·m <sup>-1</sup>
89	2500	400	160
90	3000	400	133

TABLE 5 | Types and geometric parameters of test specimens.

Specimen, mm	Bulk cylinder	Thin wall	Metamaterial segments
Height	10	10	10
Diameter/ Thickness	8	0.5; 0.75; 1; 1.25; 1.5; 2	0.5; 0.75

machining method. The NETZSCH DSC 204 F1 Phoenix device (Erich Netzsch GmbH & Co. Holding KG, Selb, Germany) with intercooler was used for the DSC analysis. Each specimen was placed in an aluminum crucible with a lid and subjected to three temperature cycles ranging from 75°C to -75°C at a constant heating and cooling rate of 10 K min<sup>-1</sup>. The test was carried out in an argon atmosphere using a flow rate of 70 ml min<sup>-1</sup>, as its lower thermal conductivity increases sensitivity in the low temperature range. An empty aluminum crucible with a lid served as reference material. The temperature was calibrated to the melting temperature of five pure substances. The NETZSCH Proteus program was used to evaluate acquired DSC data.

## 2.5 | Mechanical Properties

To determine the mechanical properties of nitinol, a cyclic compression test was performed on a Shimadzu AGX-V2 device (Shimadzu, Kjōto, Japan). In the first phase, the cylindrical specimens described in Section 2.2 were compressed in the direction parallel to the build direction (BD) until an intermediate load level of 800 MPa of engineering stress was reached, and then unloaded (the L-PBF fabricated nitinol should not reach the plastic yield point), as shown in Figure 3. In this condition, 50 loading cycles were performed at a constant strain rate of 0.001 s<sup>-1</sup> [16].

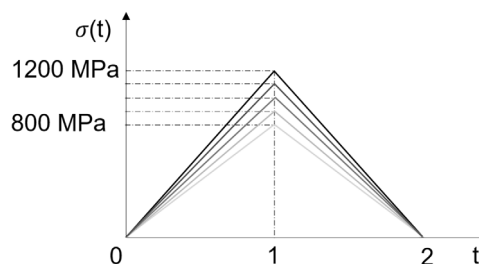


FIGURE 3 | Test parameters applied with time steps.

To allow for observation of material durability under increased stress levels with potential specimen fracture, an additional testing phase was introduced. It consisted of an additional 25 cycles with stress increasing every fifth load cycle up to 1200 MPa. The main goal of this step was to assess functional stability and observe irreversible strain accumulation triggered by martensite plasticity and dislocation slip under extreme loading conditions. Mechanical testing was carried out at room temperature.

The specimen deformation was recorded using an optical extensometer (Dantec Dynamics, Skovlunde, Denmark) based on the principle of digital 3D image correlation (DIC) with two 5 MPx cameras. The setup covered a measurement area of approximately 25 × 25 mm (base length 97.6 mm, stereo angle 27.26°). To cover the range, the system used 50 mm lenses with 10 mm intermediate rings. A customized imaging technique was used to reduce the acquired data. The correlation parameters are listed in Table 6.

The metamaterial segments were tested using the same facility. The specimens were placed freely between plates and compressed 10 times in a direction perpendicular to BD. The testing conditions are shown in Figure 4a, where applied displacement  $u_y$  from the diagram in Figure 4b was used.

## 2.6 | Finite Element Analysis

The FEA of the metamaterial segments was performed in ANSYS Workbench 23.1. (ANSYS, Canonsburg, Pennsylvania, USA) in the Static Structural module. The simulation scene was created to correspond to Figure 4a, assuming plane-stress conditions. The applied displacement  $u_y$  was obtained from Figure 4b. The 8-node planar elements with quadratic base function, known

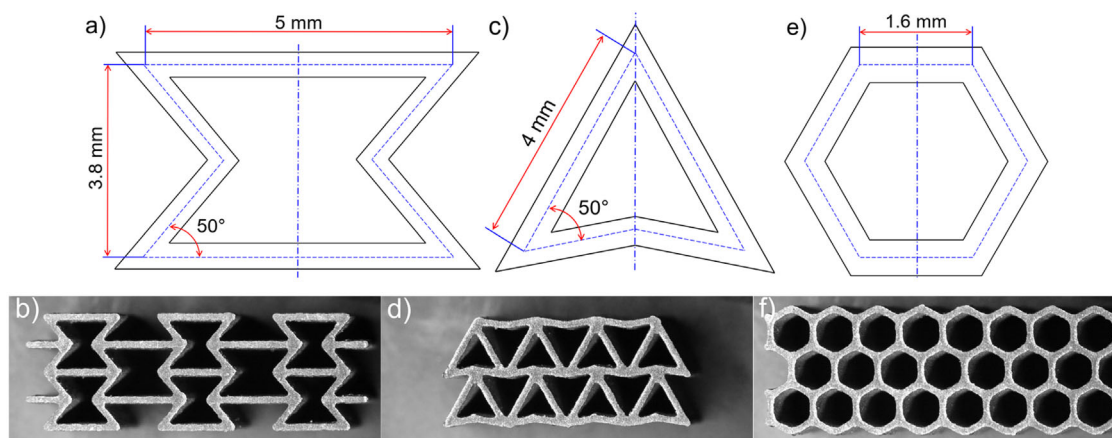


FIGURE 2 | Basic element and metamaterial segment: (a, b) re-entrant; (c, d) arrowhead; (e, f) honeycomb.

TABLE 6 | DIC correlation parameters.

Parameter	Search radius, Px	Facet size, -	Grid spacing, Px	Maximum 3D residuum, Px
Value	148	31	17	0.6

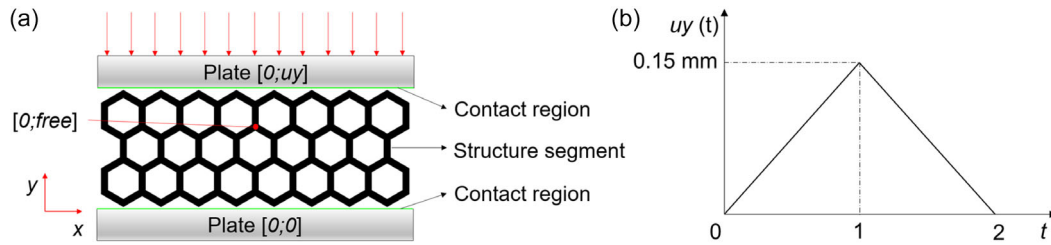


FIGURE 4 | (a) Loading scene used in the simulation; (b) loading diagram.

as PLANE 183, were used with a side length of 0.1 mm to mesh the segment and plates. A mesh convergence study was performed to ensure that further mesh refinement would not affect the accuracy of the results. The corners and the sharp edges were adapted to represent the actual state of the segments after production. Friction between bodies was set at 0.5. Poisson's ratio was set at 0.3. To define the material model, a linear elastic assumption was adopted based on the compression test of the cylinders, with the modulus of elasticity determined for each load loop separately. The purpose of this simplification of the model definition was to demonstrate the suitability of linearization in later stages of cyclic loading.

### 3 | Results and Discussion

#### 3.1 | Single-Track Experiment

In the first step, 90 single tracks were produced using process parameters defined in section 2.2. The property of the track was acquired as discrete results of microscopic measurements of the width  $W$ , height  $H$ , depth  $D$ , and contact angle  $\alpha$  (Figure 5). As expected, a decrease in scanning speed  $V$  and an increase in laser power  $P$  led to an increase in  $W$ ,  $D$ , and in some cases  $\alpha$ , while  $H$  decreased. A similar trend with close match at intermediate scanning speeds was also observed in the study by Bourke et al. when a narrower process parameter window was used [36].

A regression analysis using a quadratic polynomial function was performed to determine the relationship between the input process parameters and the resulting track properties, similar to Vaglio et al. [40]. Equation (2) represents the trend of approximate track properties ( $Z$  with  $Z \in \{W, H, D, \alpha\}$ ) as a function of the change in scan velocity ( $V$ ) in  $\text{mm s}^{-1}$  and laser power ( $P$ ) in  $W$ . In addition, a continuous prediction of the track properties was made based on possible combinations of input parameters. The polynomial parameters of the regression function ( $\beta_0 \dots \beta_5$ ) are given in Table 7. Low mean square error shows that a better approximation and thus a potential trend estimation were achieved for the track width and depth. The poorer approximation of the track height can be attributed to the wide window of process parameters, which in extreme cases led to considerable melt pool pulsations and a balling effect. Large variations in the

measured height led to a deviation from the plane that approximates the data set, even when a second-order polynomial function was used. Based on the observations, process parameters that result in discontinuous or significantly cracked tracks were excluded from further trials. In addition, parameter combinations that resulted in keyhole porosity or excessively low or even unmeasurable melting depths were also not considered. The last selection criterion applied setup an  $\alpha$  angle limit to minimum of  $100^\circ$  to avoid the balling effect. Closer consideration of  $\alpha$  and  $H$  in the selection process was not considered because of the low values of the determination coefficient in the model.

$$Z = \beta_0 + \beta_1 V + \beta_2 P + \beta_3 V^2 + \beta_4 P^2 + \beta_5 VP \quad (2)$$

#### 3.2 | Investigation of Internal Composition

Based on the parameters mentioned in Section 3.1, 12 groups of process parameters were selected for further investigation of internal homogeneity (Table 8). The parameters were assigned with a hatch distance and used to produce cylindrical specimens. The following equation was used to determine the VED delivered to the powder layer during the manufacturing process:

$$\text{VED} = \frac{P}{V \cdot H \cdot L} [J \cdot \text{mm}^{-3}] \quad (3)$$

where  $H$  is the hatch spacing, and  $L$  is the layer thickness.

The internal homogeneity analysis of the cylinders showed low internal porosity (Figure 6), but some of the produced specimens were prone to macroscopic cracking after fabrication (Figure 6 detail). A similar phenomenon was also described in the literature for process parameters resulting in comparable VED [30]. Maximum internal porosity of 0.24% was observed for  $V$  at an intermediate value of  $1000 \text{ mm s}^{-1}$ ,  $p = 400 \text{ W}$ , and a high value of  $H = 125 \mu\text{m}$ , resulting in a peak VED of  $64 \text{ J mm}^{-3}$ . In contrast, the lowest internal porosity of less than 0.1% was achieved when  $H$  was reduced to  $105 \mu\text{m}$  and  $P$  to  $280 \text{ W}$ , resulting in a VED of  $53.3 \text{ J mm}^{-3}$ . The more comprehensive comparison with review literature, where different process parameters and Ni contents were considered, resulted in a higher relative density of the material [30, 41]. The only comparable density was obtained with a VED of  $41 \text{ J mm}^{-3}$  with a similar Ni content and similar parameters [42]. In general, a very high relative density was achieved

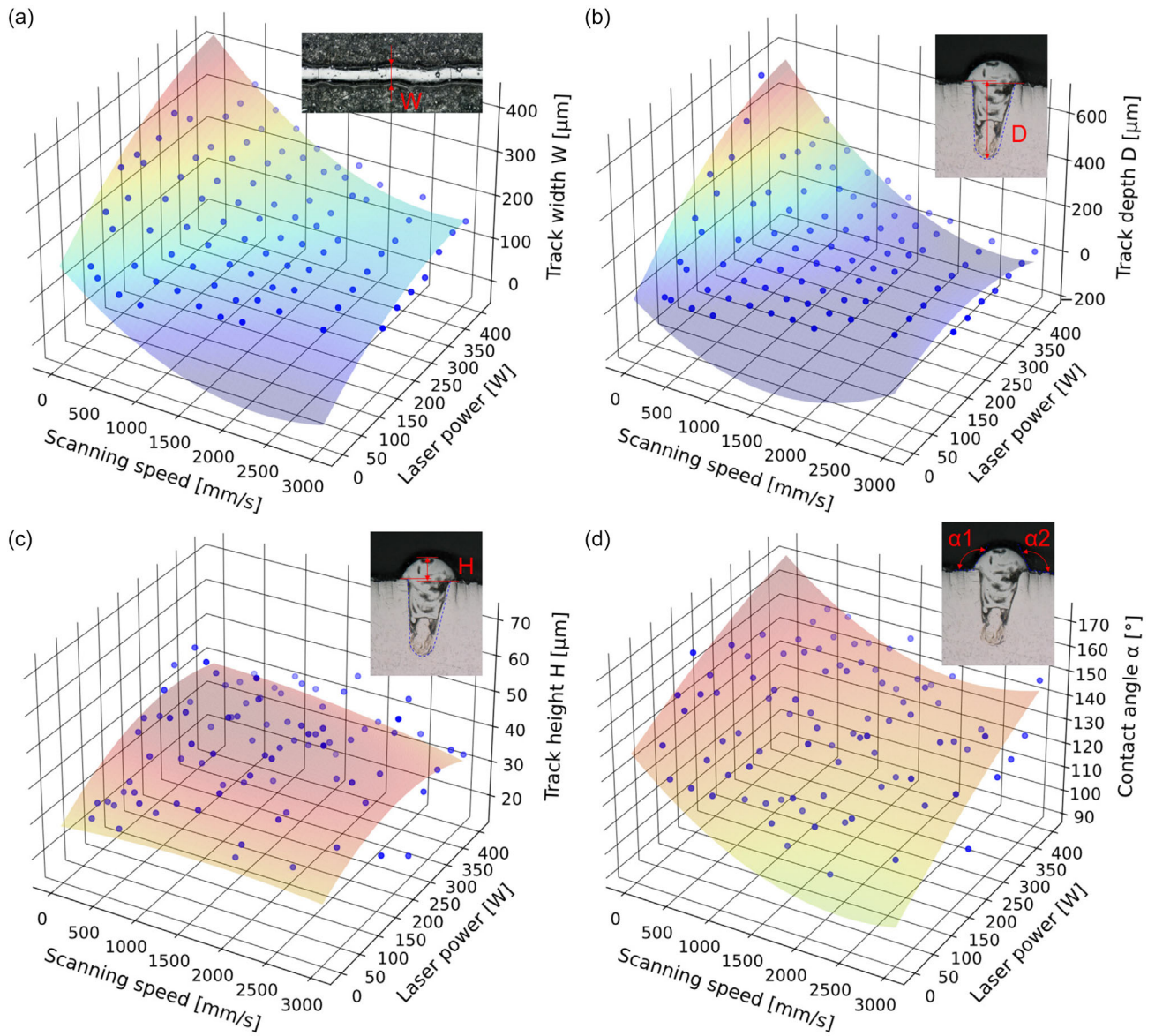


**FIGURE 5** | Dependence of the single track (a) width, (b) depth, (c) height, and (d) contact angle on the scanning speed and laser power.

**TABLE 7** | Quadratic regression coefficients and intercept; MSE and  $R^2$  are the mean square error and coefficient of determination, respectively.

Property	Intercept	Coefficients					MSE	$R^2$
	$\beta_0$	$\beta_1$	$\beta_2$	$\beta_3$	$\beta_4$	$\beta_5$		
Track width	1.61e2	-1.58e-1	1.05e0	3.49e-5	-9.12e-5	-1.03e-3	584.32	0.90
Track depth	5.79e1	-2.93e-1	2.26e0	8.88e-5	-4.28e-4	-2.48e-3	1940.1	0.85
Track height	3.72e1	1.90e-3	9.22e-2	-6.51e-7	-9.82e-6	-1.78e-4	128.27	0.05
Contact angle	1.35 e2	-3.12e-2	1.24e-1	6.63e-6	4.93e-6	-7.53e-5	154.35	0.29

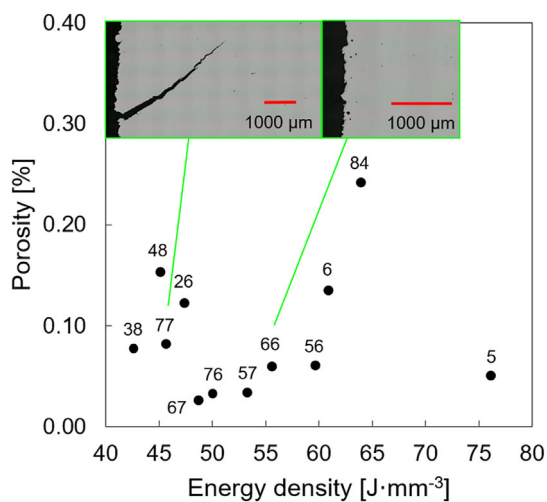
for VED in the range of  $41\text{--}55\text{ J mm}^{-3}$  in the present study, with an internal porosity of less than 0.25%. However, it is worth noting that the layer thickness used in the source study was only  $30\text{ }\mu\text{m}$ . Furthermore, some of the specimens showed an excessive number of pores in subsurface regions, which excluded them from further analyses. The remaining three parameter setups (Table 8) 38, 56, and 76 were designated as A, B, and C, respectively.

### 3.3 | Phase Transformation Behavior

Figure 7a shows the first cycle of DSC measurement on selected specimens in as-build condition. The heating of the specimen to  $+75^\circ\text{C}$  and subsequent cooling to  $-75^\circ\text{C}$  caused an endothermic and an exothermic peak in the curve. During the forward transformation from austenite to martensite, the corresponding exothermic peak indicated a direct single-step transformation

**TABLE 8** | Selection of the L-PBF process parameters to produce specimens.

Parameter	Laser Power P, W	Scanning speed V, mm · s <sup>-1</sup>	Hatch distance H, μm	VED, J · mm <sup>-3</sup>
5	80	175	120	76.2
6	80	250	105	61
26	160	750	90	47.4
38	200	1250	75	42.7
48	240	1250	85	45.2
56	280	750	125	59.7
57	280	1000	105	53.3
66	320	1000	115	55.7
67	320	1250	105	48.8
76	360	1250	115	50.1
77	360	1500	105	45.7
84	400	1000	125	64

**FIGURE 6** | Comparison of the internal porosity of the cylinders (6x8 mm area).

without the occurrence of the R-phase [15, 39]. The heating curve also showed a reverse single-step transformation indicated by the endothermic peak. Note that the exothermic peak occurred at the edge of the measured temperature interval, making it impossible to estimate the end of the martensitic transformation. The broad and flat shape of the curve indicated a slow and weak transformation, which is attributed to the high dislocation density of the L-PBF process.

Figure 7b shows the characteristic temperatures  $A_s$ ,  $A_p$ , and  $A_f$  (start, peak, and end of austenite transformation during heating) as well as  $M_s$  and  $M_p$  (start and end of martensite formation during cooling) compared to the initial state of the powder. The powder material measurement showed a purely superelastic behavior at conditions far above room temperature (at 31°C). In contrast, all configurations produced at room temperature were considered superelastic, as the endothermic reaction  $A_f$  ended below 20°C. Accordingly, a comparison of the martensitic transformation of the as-built specimen showed that the onset of the exothermic reaction in the group A and group C configurations began at lower  $M_s$  temperatures. The results are in line with

the study of Zhang et al. [12], who reported a complex relationship, observing that transformation temperatures increased with VED up to a critical value of approximately 100 J mm<sup>-3</sup>, beyond which further VED increase produced minimal additional shifts.

### 3.4 | Compression Test

The cyclic loading was evaluated by two main characteristics—recoverable strain ( $\epsilon_{rec}$ ) [43] and critical stress to initiate stress-induced martensitic transformation ( $\sigma_{SIM}$ ) [41]. The first phase of the cyclic compression of the cylinders did not show a clear plateau region (Figure 8), but the initial loading cycle indicated the stress level where the martensitic transformation  $\sigma_{SIM}$  started. It can be concluded that the higher  $\sigma_{SIM}$  was present, the higher the total deformation strain at the load peak  $\epsilon_{tot}$  was observed, ranging from 460 MPa at configuration C to 525 MPa at configuration B. With an increasing number of loading cycles, stress hysteresis dropped as the irrecoverable strain accumulated due to retained stabilized martensite and/or plastic deformation [44].

A variable superelastic response with the highest total strain of 5.43% at the 50<sup>th</sup> cycle for configuration B (Figure 9a), while the lowest total strain was observed for configuration C at only 4.65%. The most significant decrease in recoverability was observed in group B, where the cumulative residual strain reached 2.79% after 50 cycles. A comparison with additively manufactured nitinol specimens described in the literature and tested under similar conditions showed that configuration B achieved a similar stiffness, resulting in a higher total strain at maximum load at the 50<sup>th</sup> cycle [45, 46]. According to Liu et al. [47], one possible reason for this was the nanocrystalline/amorphous dual-phase structure that occurred in mechanically cyclized L-PBF fabricated nitinol. Furthermore, it was reported that an increase in scanning speed, which resulted in deformation of the melt pool, led to a reduction in the transformation temperature and an increase in the transformation interval. This was also confirmed in the current study, where a decrease in transformation temperature was observed for groups A and C at higher scanning speed (from 750 mm s<sup>-1</sup> for B to 1250 mm s<sup>-1</sup>). Another study indicated that the build orientation of the tested specimen also plays an important role in hysteresis and superelastic recovery [48].

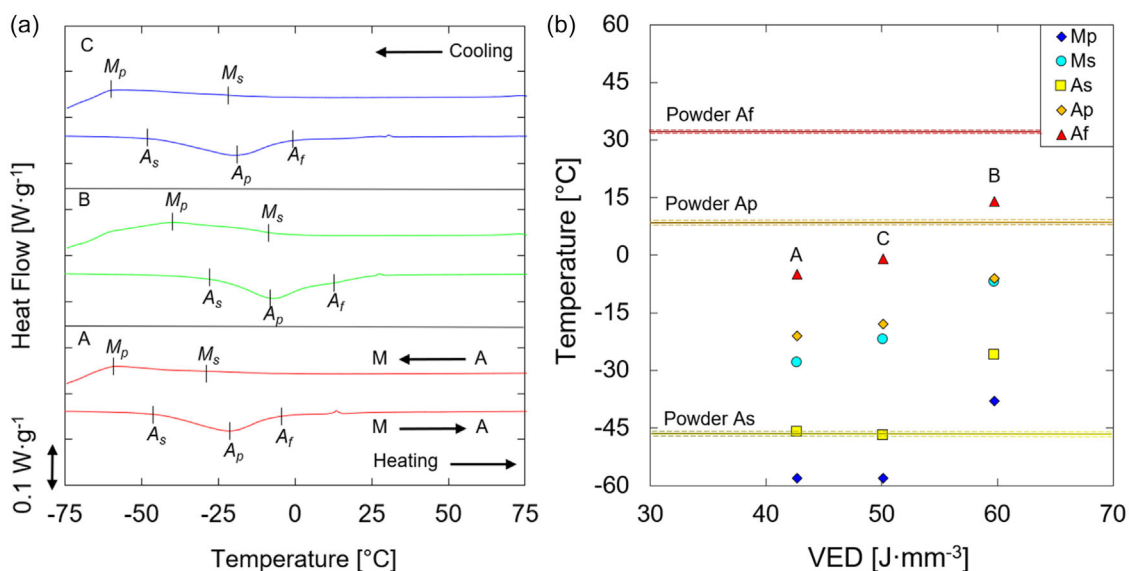


**FIGURE 7** | (a) DSC curves of selected specimens showing change in transformation temperatures as a function of the L-PBF processing parameters; (b) Summarized phase transformation temperatures compared to the powder measurement (depicted by horizontal lines, standard deviation depicted by dashed lines).

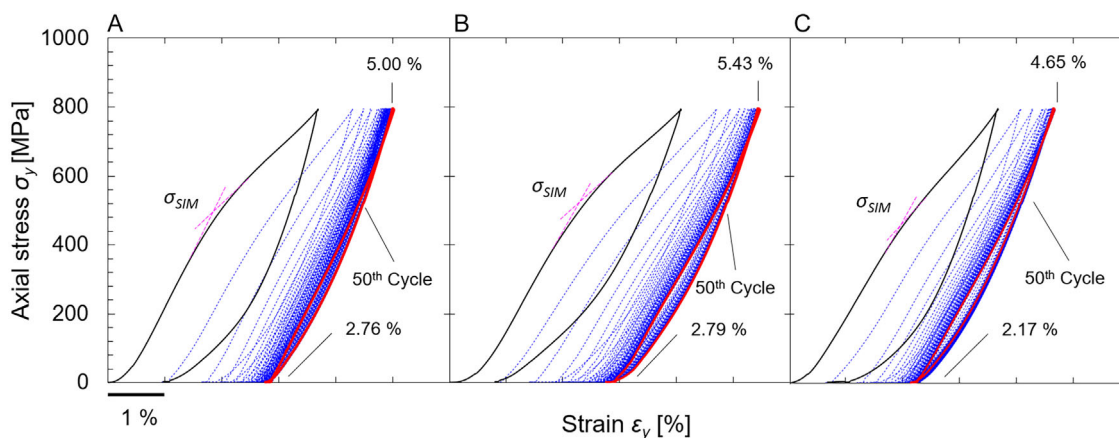


**FIGURE 8** | Stress-strain curves of superelastic nitinol at 50 cycles.

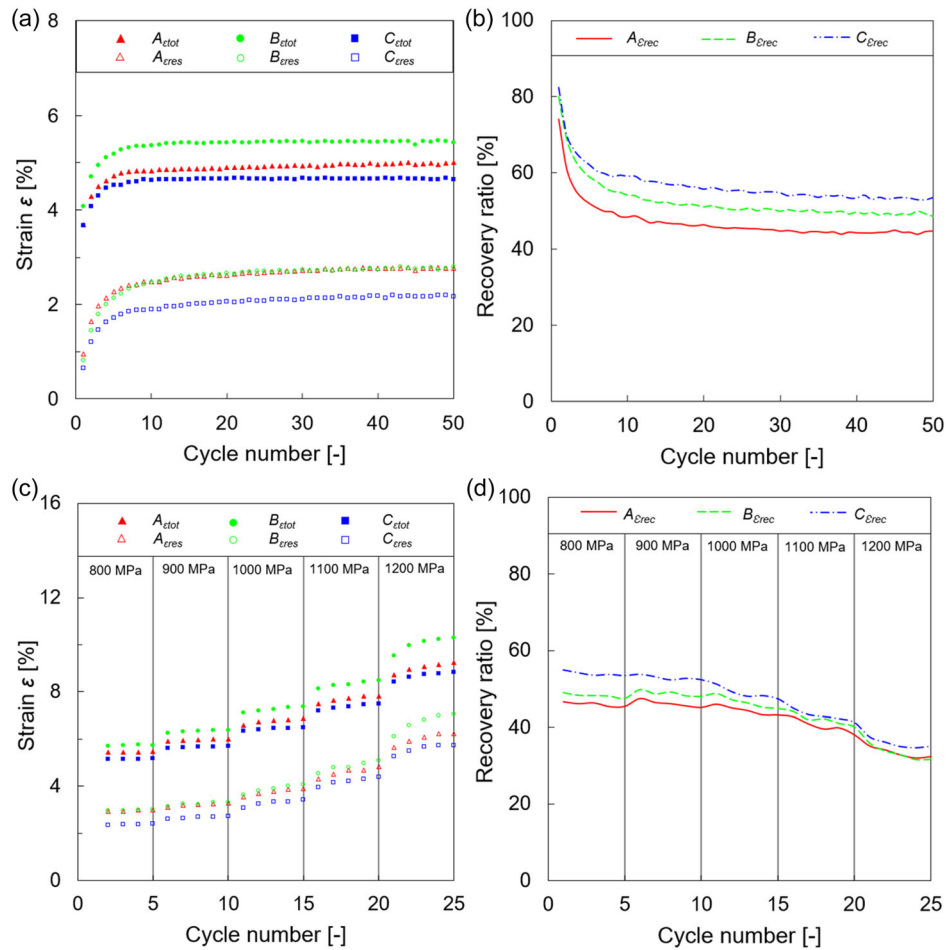
In all specimen groups observed, the deterioration in recovery and the rapid change in hysteresis were most pronounced in the first cycles, leading to a narrowing of the loop until the difference between the loading and unloading pathways almost disappeared (Figure 8). Linearization of the hysteresis loop was also previously observed [49, 50], indicating a limitation of additively manufactured nitinol for applications where large repeating deformations are expected. According to recent studies, the increase in irrecoverable strain is attributed to high residual stress and microstructural defects such as pores and cracks. It increases dislocation density, which changes a strong first-order transition to a weak first-order or continuous transition [51, 52]. Clarification of the underlying mechanisms for this type of behavior plays an important role in the development of programmable metamaterials.

Figure 9a shows the maximum total strain ( $\epsilon_{tot}$ ) and the cumulative residual strain ( $\epsilon_{res}$ ) for the tested configurations. The load loops were considered stabilized if at least five adjacent cumulative  $\epsilon_{res}$  showed a difference of less than 0.01%. According to this

criterion, the observed trend of material recovery showed stabilization at the 38<sup>th</sup> cycle for groups A and B and stabilization at the 36<sup>th</sup> cycle for group C. This was consistent with the results described in a previous study, where stabilization was observed between the 30<sup>th</sup> and 40<sup>th</sup> cycle for conventionally produced nitinol wires [19]. In contrast, in another source study, stabilization of nitinol produced by selective laser melting in the as-fabricated state was observed as early as the 10<sup>th</sup> cycle [18].

However, it is important to emphasize that the cyclic test in the source study was terminated after the 10<sup>th</sup> cycle, and the stabilization criterion differed from the current study. Despite the difference in stabilization recognition, the  $\epsilon_{rec}$  in the 10<sup>th</sup> cycle was in the range of 2.34% and 2.9%, which was comparable to the source study.

Further observations showed that additional cyclic loading led to a slow deterioration of nitinol in the form of a continuous reduction in  $\epsilon_{rec}$  and hysteresis to a quasilinear form. It was measurable in all tested groups, regardless of the process parameters used, until the last experimentally tested cycle. The recovery ratio was used as an indicator (Figure 9b), expressed as the



**FIGURE 9** | (a) Maximum total and cumulative residual strain in 50 cycles of 40 kN load; (b) recovery ratio in 50 cycles of 40 kN load; (c)  $\epsilon_{tot}$  and  $\epsilon_{res}$  in an additional 25 cycles with increased load; (d) recovery ratio in an additional 25 cycles with increased load.

ratio between the cumulative  $\epsilon_{res}$  and the  $\epsilon_{tot}$  in percent [11]. Configuration C achieved the highest recovery ratio, 82.4% in the 1<sup>st</sup> cycle and 53.4% in the 50<sup>th</sup> cycle. Similar behavior, including the reduction in hysteresis, was also observed in previous studies testing conventionally manufactured nitinol wires [21, 44]. However, it appeared that fewer loading cycles were required to achieve a significant reduction in hysteresis and  $\epsilon_{rec}$  in specimens prepared with L-PBF [11]. The offset in stabilized values of  $\epsilon_{rec}$  between the tested groups in the first phase at intermediate load with 800 MPa engineering stress was attributed to different process parameters (Table 8) and was associated with a slight change in transformation temperatures (Figure 7b) between all groups. The second test phase with an increase in maximum load (Figure 9c) showed a persistent trend of reduction in cumulative  $\epsilon_{res}$  in the unloaded state, indicating continued degradation of the material without obvious changes in behavior. It should be noted that both the cumulative  $\epsilon_{tot}$  and the cumulative  $\epsilon_{res}$  measured at the corresponding loading intervals increased more rapidly, with the trend amplifying at the higher loads. In this respect, configuration B was shown to be the most affected by the higher loads, as it reached the highest  $\epsilon_{tot}$  of 10.3% at 1 200 MPa, but is also the most prone to deterioration (cumulative  $\epsilon_{res}$  of 7.0%). At intermediate load, the offset in recoverable strain between the tested groups remained the same in the later stages of loading. As the load increased to a high level, the difference in  $\epsilon_{rec}$  decreased

and stabilized the offset between groups. Interestingly, the recovery ratio of configuration B dropped to 31.6% (Figure 9d), which was the same level as configuration A. Although configuration C had the lowest  $\epsilon_{tot}$ , its recovery ratio was better in both phases of the test. This indicates that the recovery ratio depends on the load, and the offset between the  $\epsilon_{rec}$  of different groups is mitigated at high loads. This implies that for engineering applications, stabilization at the intended load must be performed before commissioning L-PBF fabricated components for service.

### 3.5 | Microstructural Characterization

The inverse pole figure (IPF) color-coded EBSD maps (see Figure 10a,c) showed the as-built structure in cross-sections along and perpendicular to BD. The structure reflected highly directional solidification and grain growth, resulting in a significantly textured microstructure with elongated columnar grains. This phenomenon stemmed from steep thermal gradients during the layer-by-layer melting process, where grains grew and solidified perpendicular to the pool boundary towards the centerline of the melt pool [53–55]. This was also reflected in complex and irregular grain morphology. Corresponding pole figures (Figure 10e) confirmed a pronounced {100} texture along the BD, which was frequently reported for alloys with cubic-centered crystal lattices produced by L-PBF [56]. This crystallographic

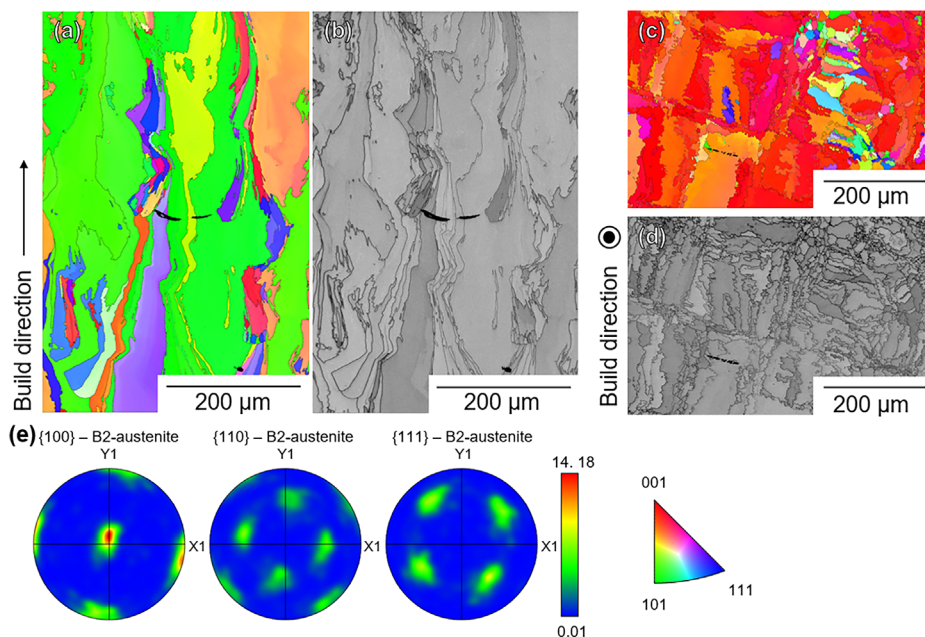


**FIGURE 10** | Observation of the nitinol specimen of group C in the as-built state: (a) IPF Y – crystallographic grain orientation in the BD; (b) band contrast map in the BD; (c) IPF Z – crystallographic grain orientation in the plane perpendicular to the BD; (d) band contrast map in the plane perpendicular to the BD; (e) volume fraction distribution of austenite.

texture is known to influence the anisotropic mechanical and functional properties of nitinol, including the orientation dependence of the martensitic transformation and the superelastic behavior of the alloy.

The IPF shows a section perpendicular to the BD in which the grain boundaries correspond to the  $67^\circ$  orientation angle of the interlayer paths (Figure 10d). The figure shows wrinkled grain boundaries in contrast to conventionally produced nitinol, which crystallizes directly from the melt pool [57, 58].

Comparison of the as-built microstructure (Figure 10) and after cyclic loading (Figure 11) illustrated distinct changes. The original columnar grains appeared fragmented, with signs of grain subdivision and increased intragranular misorientation. These changes indicated the accumulation of plastic strains and  $\sigma_{SIM}$  [41, 59, 60]. The columnar grain structure remained partially visible but was disrupted by the formation of subgrains and deformation bands. Interestingly, some of the grains did not

tend to have deformation bands, while some bands were present in several neighboring grains (Figure 11b,e). This increased heterogeneity in crystallographic orientation indicates strain localization and dislocation activity typical of nitinol under cyclic strain [61, 62]. Phase analysis revealed localized martensitic transformations within deformation bands (Figure 11c,f) characterized by strong local misorientation and disturbed crystallographic alignment, which act as preferential sites for  $\sigma_{SIM}$ . The strong granular texture indicated by the intensity peak in  $\{100\}$  in Figure 10e was not confirmed after cyclic loading. Instead, weaker and more diffuse intensities can be observed in all directions. The transmission Kikuchi diffraction (TKD) map (Figure 12) confirmed fine martensite laths embedded in deformation bands. Variants of B19' martensite can be recognized by their different orientations, which depend on the orientation of the grain with respect to the loading direction. In addition, a band contrast map (Figure 12b) indicated that the

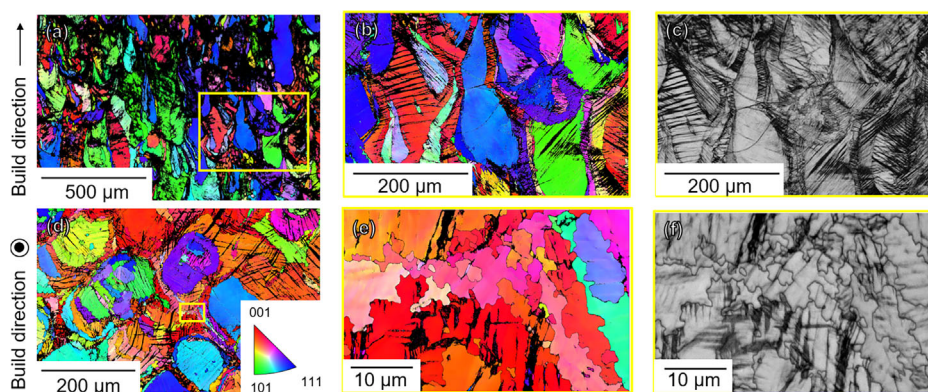


**FIGURE 11** | Observation of nitinol specimens of group C after cyclic loading: (a) IPF Y: crystallographic grain orientation in BD; (b) IPF Y: magnification of the deformation bands; (c) band contrast map in the BD; (d) IPF Z: crystallographic grain orientation in the plane perpendicular to the BD; (e) IPF Z: magnification of the deformation bands; (f) band contrast map in the plane perpendicular to the BD; (g) volume fraction distribution of B2.

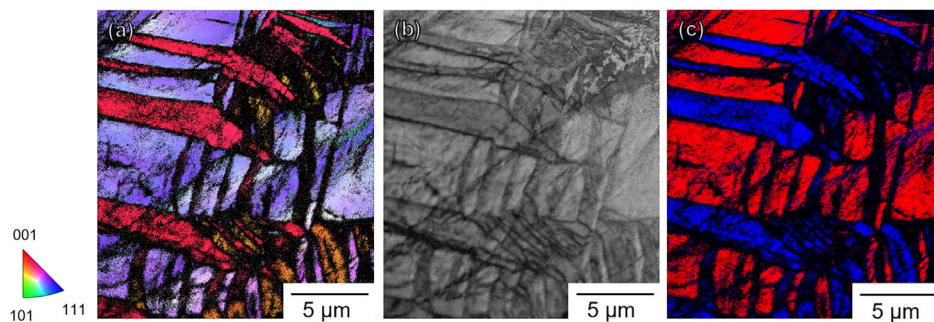


**FIGURE 12** | TKD of nitinol specimen of group C after cyclic loading: (a) IPF X: crystallographic grain orientation in BD; (b) band contrast map; (c) phase map (red: B2 austenite, blue: B19' martensite).

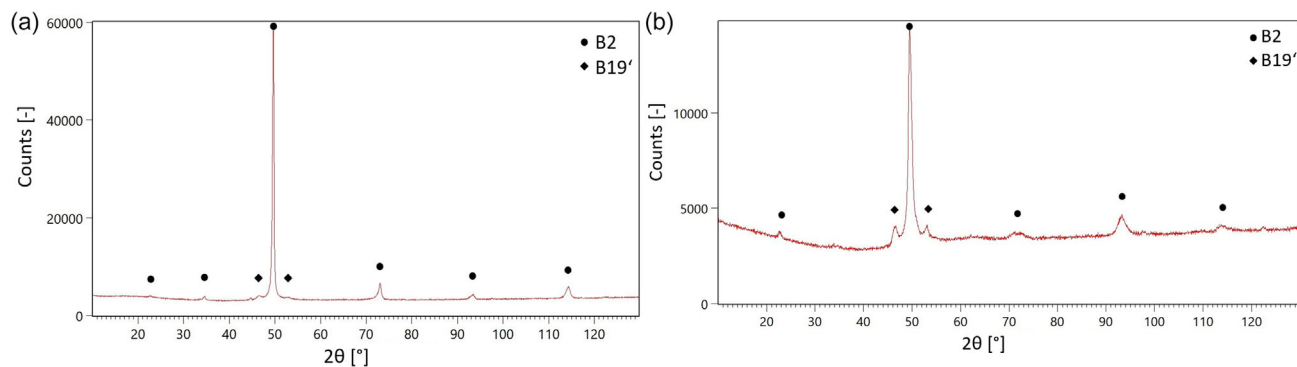


**FIGURE 13** | XRD pattern for the specimen of group C in (a) as-built state; (b) after cyclic loading.

deformation bands contained a high dislocation density. The presence of residual martensite in these areas indicated a partial irreversibility of the transformation process. The observation was consistent with functional fatigue mechanisms such as transformation-induced plasticity and dislocation locking [61]. Such microstructural evolution was closely related to the degradation of superelastic performance, as described in Section 3.4.

The quantification of the phases by X-ray diffraction (XRD) supported microstructural observations. After cyclic loading, a significant reduction in the B2 austenite phase fraction from 97.7% to 91.5% and an increase in B19' martensite from 2.3% to 8.5% was observed (Figure 13). This phase development indicated that part of the parent phase was irreversibly transformed into martensite by the cyclic mechanical stress [63, 64]. This retained martensite, especially when stabilized by dislocation structures or local inhomogeneities in the composition, may degrade the superelastic response and reduce the reversibility of the SME in service [65, 66].

### 3.6 | Thin Walls Analysis

Based on Section 3.2, the process parameters characterized by low internal porosity and the absence of cracks in the bulk cylinders (Table 8) were selected for further investigation in the form of thin-walls with a nominal thickness of 0.5–2 mm. Figure 14a shows a 0.5 mm thick specimen with a measured mean thickness below the nominal value, while Figure 14b shows a 2-mm thick specimen with a mean thickness above the nominal value. The range of the measured data in Figure 14b, expressed by three

times the standard deviation, was significantly larger than that of the data in Figure 14a, indicating that the variation in manufacturing dimensions increased when higher nominal thicknesses were used.

Figure 15 shows a general comparison of the mean measured thicknesses compared to the nominal values. It can be clearly seen that the measured specimens tended to be thinner at a nominal value of 0.5 mm, regardless of the group. The lowest measured thickness was observed for group B with a mean value of 465  $\mu\text{m}$ . With this exception, the measured thickness was greater than the nominal thickness. The largest thickness deviation was measured at a nominal thickness of 2 mm with a maximum value of 2148  $\mu\text{m}$  for group C (Figure 15a). However, the smallest thickness deviations were found for group A across the entire range of nominal thicknesses tested. This indicates that a potential design of metamaterial based on the process parameters of group A would fit the best a real state of the produced geometry. It should be noted that the range of three times the standard deviation of the measured thickness does not overlap with the nominal thickness at 1.5 and 2 mm. Surprisingly, thicker walls led to larger deviations, but these were more uniform in thickness variation. The mechanism responsible for the different wall thickness deviations in the different groups could be attributed to the different energy density supplied to the melt pool, as well as the lower heat dissipation path for thinner walls [67, 68]. Higher melt pool temperatures were expected for them, which led to fewer adhering particles. As a result, thicker walls tended to have greater thickness due to more adhering particles. Another parameter that played a key role here was the scanning strategy, which influenced the mutual position of the contours and the

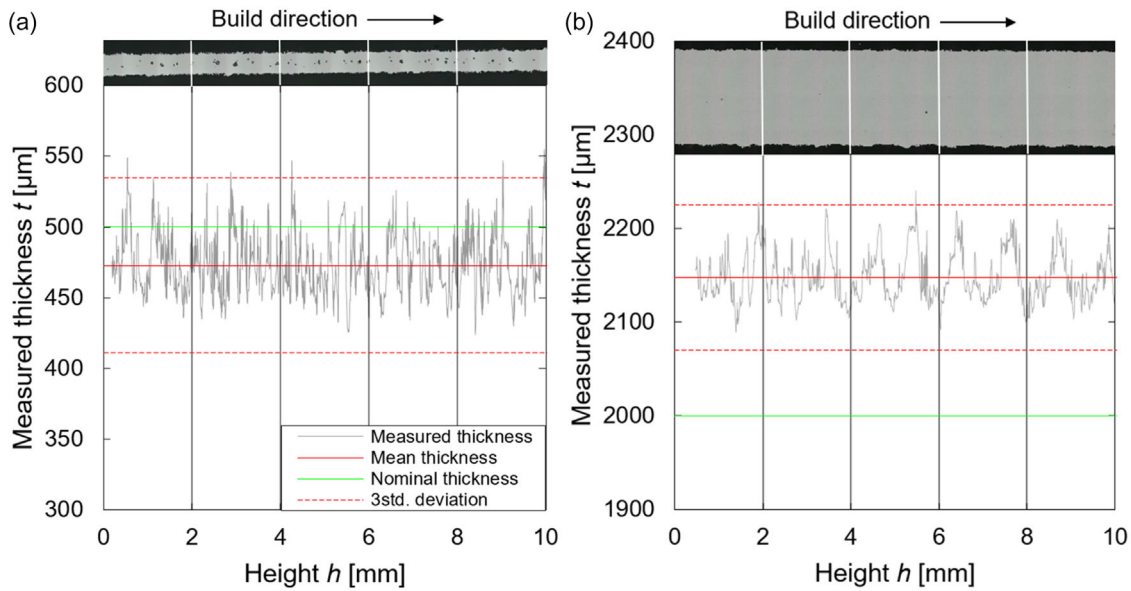


**FIGURE 14** | Dimensional analysis of the thin wall of (a) group A with a nominal thickness of 0.5 mm; (b) group C with a nominal thickness of 2 mm.

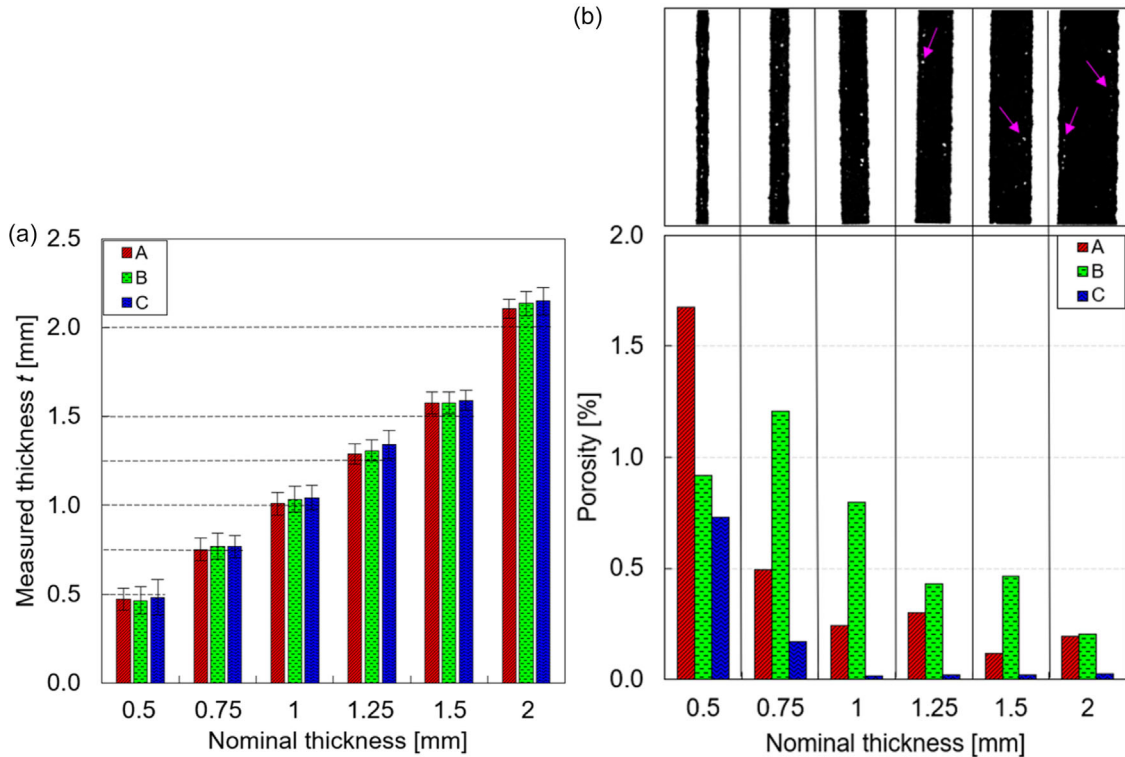


**FIGURE 15** | (a) Measured wall thickness (error bars represent three times the standard deviation); (b) total porosity of the walls.

scan vectors used for the core hatching [50, 51]. Furthermore, as a result of the sliced geometry, some of the very short vectors could be omitted when the laser passed the scan path, especially in the case of very thin walls.

The results of the measurement were further used to adjust the geometry model to get a realistic shape in the FEA of thin walls in the metamaterial segments.

The total porosity for thin walls produced with the above-mentioned groups of process parameters is shown in Figure 15b.

It can be assumed that a higher total porosity can be observed for thin walls with a lower nominal thickness. Total porosity reached 1.68 % for group A, with a nominal thickness of 0.5 mm, and decreased irregularly with increasing nominal wall thickness. An approximately similar trend can also be observed for groups B and C, indicating that the influence of subsurface porosity was particularly strong for thin specimens. One possible cause could be the heat dissipation in the built direction, which was dominant. In consequence, the melt pool became deeper with

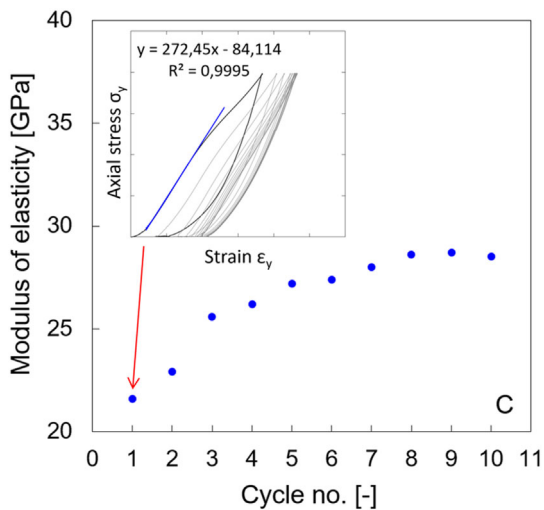


**FIGURE 16** | Modulus of elasticity used in FEA of metamaterials segments in individual cycles.

decreasing thickness and promoted the formation of keyhole pores, leading to increased subsurface porosity [67]. In general, the pores in this experiment occurred in chains in subsurface

areas at all heights (Figure 15b violet arrows). This effect was attributed to the increased evaporation of metal because of changes in scan velocity during the slowdown of the laser spot reversal at the end of each track [69]. For thin walls, where very short hatch tracks were generated, this effect was even more detrimental.

### 3.7 | Metamaterial Segments

Based on the highest recoverability observed in the previous section and the lowest subsurface porosity of thin walls, the process parameters used to produce configuration C were chosen to produce metamaterial segments. The geometry model was prepared incorporating the deviations detected in Section 3.6. The material model was prepared using the modulus of elasticity determined separately for each loading cycle based on the compression test of the cylinders of the same group (Figure 16). This step was decided due to the cyclic strain hardening behavior of nitinol reported in the metamaterial specimens tested, which showed significantly higher stiffness than the numerical results for validation in the 10<sup>th</sup> loading cycle [8]. Figure 16 confirms these findings expressed in terms of elasticity modulus change, with the most

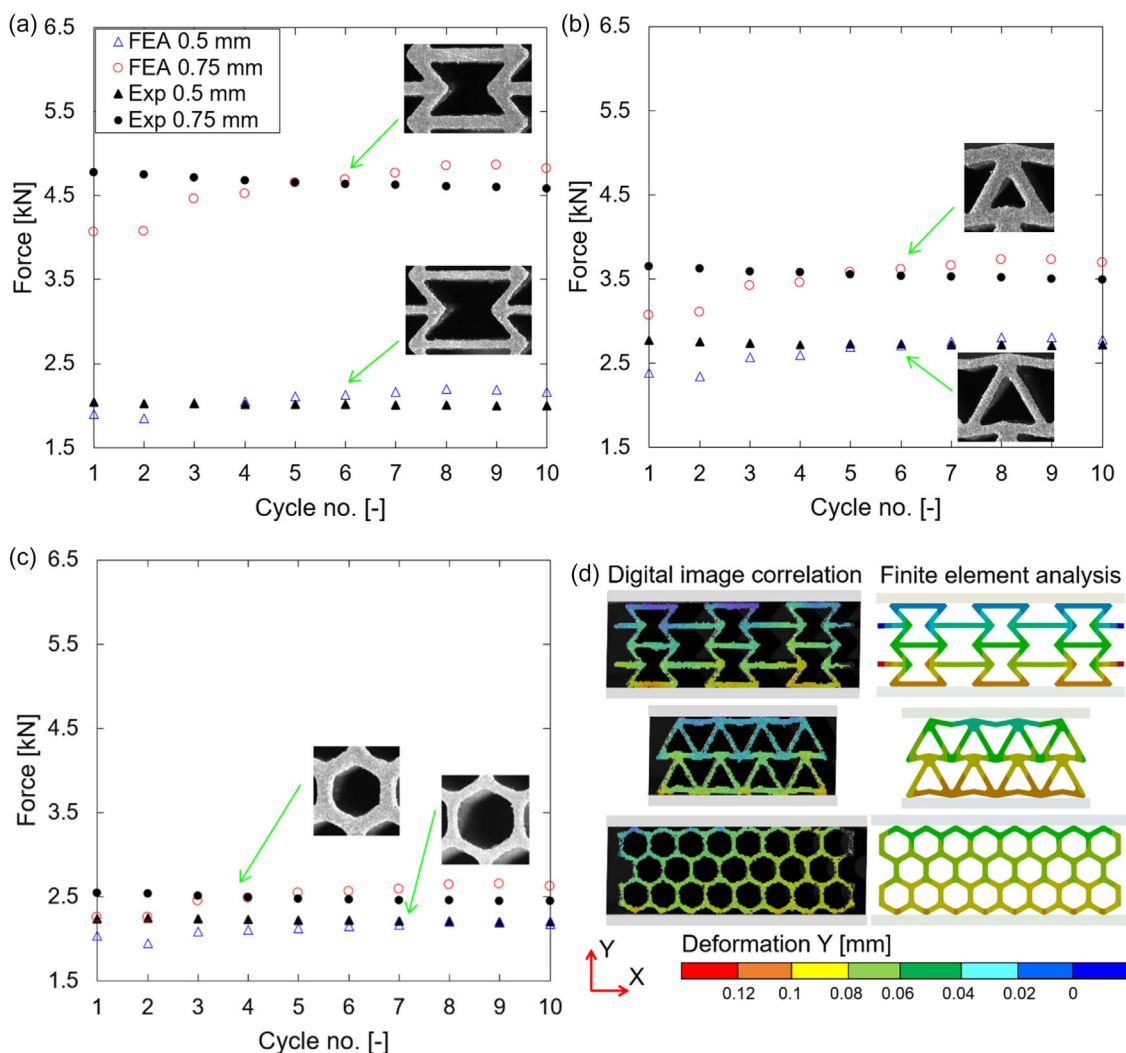


**FIGURE 17** | Peak force reaction of metamaterial segment under cyclic loading – experiment vs FEA for (a) re-entrant; (b) arrowhead; (c) honeycomb; and (d) qualitative comparison for nominal wall thickness of 0.5 mm.

significant difference between the 1<sup>st</sup> and 3<sup>rd</sup> cycle. Together, the modulus of elasticity changed from 21.6 to 28.5 GPa within 10 cycles. The values obtained were used for the parametric computations described in this section.

Figure 17a,c shows a comparison of the force reaction of individual segments of the metamaterial. For each geometry, the change in nominal wall thickness caused different reaction shifts, where Figure 17a shows nearly two times higher values when the wall thickness increased, while Figure 17c tends to minimal changes. This was to some extent given by the ratio of unit cells in the vertical and horizontal directions, their size, and arrangement in the metamaterial segment. However, all geometries tested in the experiment had a common trend of declining force in a range of 2–4 % between the first and the tenth cycle. This trend is attributed to a phenomenon related to the deterioration of recoverability previously observed for cylinders. Similar behavior was described by Yan et al. [8] who investigated spatial metamaterials made of nitinol. In addition, irregular deformation distribution predicted by FEA and validated by DIC (Figure 17d) is attributed to variation of loading history across specimens, which indicates continuous deterioration without early stabilization.

Comparison with simulation showed consistency across all computationally determined results, indicating an underestimation of the stiffness of the metamaterial in the first several loops of cyclic loading. However, with an increasing number of cycles, the prediction of the force reaction got closer to the experimental results. This effect was attributed to changes in the history of loading of the material described for the cylinders (Figure 8) from which the modulus of elasticity in the FEA was derived. Changes manifested in narrowing hysteresis loops with an increasing number of loading cycles, where the difference between the loading and unloading pathways was nearly negligible. It allowed the use of a relatively simple material model definition with linear elastic assumption, resulting in a good accuracy of prediction in a later stage of cyclic loading. On the other hand, based on diagrams in Figure 17a,c, it can be concluded that initial performance in the initial stages of cyclic loading requires using a sophisticated definition of material model, like one proposed by Auricchio et al., where a nonlinear definition of loading and unloading pathways of the hysteresis loop would fit better [4]. It would, however, lead to higher computational efforts coming out of convergence issues induced by strong material nonlinearities.

Note that when designing components with a small number of load cycles, the simple material model used enables a good prediction of the behavior even for complex metamaterial structures. This approach may also be suitable for components in space applications with a known number of load cycles over the lifetime of the component. For example, it could be used for the development of new separation systems for small satellites with limited dimensions and weight, to ensure 100% functionality for a single payload separation is essential. Only a limited number of element-level tests (tens) and 2–3 qualification tests of the functional system are performed before launch. Despite the high degree of degradation of the recoverable strain (recovery ratio approx. 50%), additively manufactured NiTi structures still offer very attractive values for the usable deformation (approx. 2.5%) and thus provide an opportunity for weight reduction.

## 4 | Conclusion

A wide range of L-PBF processing parameters was tested to produce a Ni50.7Ti49.3 alloy suitable for metamaterial morphing applications, resulting in three setups with excellent properties. An internal porosity in specimens produced with selected setups was less than 0.1%, without macroscopic cracks. The highest  $A_f$  transformation temperature measured was 14°C, which clearly indicates a purely superelastic behavior at room temperature. The mechanical and microstructural properties of the parent material were observed under cyclical loading, with a maximum recoverability drop not exceeding 53%. The recoverability estimation of the metamaterial proved high fidelity when actual parent material conditions were incorporated into the material and geometry model. The main results can be summarized as follows:

1. The three parameter configurations selected with VED ranging from 42.7 to 59.7 J mm<sup>-3</sup> led to different levels of  $\epsilon_{rec}$ , with an absolute difference of around 0.7% within the groups studied.
2. During cyclic loading, the superelastic performance deteriorated considerably. The deterioration in recovery strain and the rapid change in the shape of the loading loop were most significant in the first 5 cycles. The observed trend of material deterioration stabilized on average after 30 cycles in the tested groups.
3. No clear plateau region was observed for load loops, but initial loading cycles indicated the  $\sigma_{SIM}$  ranging from 460 to 525 MPa. With an increasing number of load cycles, the hysteresis tended to reduce to a quasilinear pseudoelasticity.
4. The recoverable strain decreased with increasing load. From a recovery ratio of 53.4% at an intermediate load level of 800 MPa to 35.1% at a high load level of 1200 MPa.
5. TKD after cyclic loading confirmed fine martensite laths embedded in deformation bands, indicating a high dislocation density. A significant decrease in the austenite phase fraction of B2 from 97.7% to 91.5% and an increase in B19' martensite from 2.3% to 8.5% was observed. The presence of residual martensite in these areas indicated a partial irreversibility of the transformation process.
6. Cyclic compression of metamaterial segments showed a decreasing tendency for force response in a range of 2–4% between the first and the tenth cycle, according to the observations on bulk specimens. The irregular distribution of deformation across the structure predicted by FEA was confirmed by DIC.
7. Simulation of metamaterial segments using a simplified material model with experimentally determined variable modulus (21.6–28.5 GPa) and actual wall thickness allowed accurate estimation of the force response after the fifth cycle.

### Author Contributions

**Ondřej Červinek:** conceptualization (lead); data curation (lead); formal analysis (lead); investigation (lead); methodology (lead); software (lead); validation (lead); visualization (lead); writing—original draft (lead);

writing—review & editing (lead). **Jakub Hurník**: formal analysis (supporting); investigation (supporting); methodology (supporting); software (supporting); validation (supporting); writing—original draft (supporting). **Miroslav Šmid**: formal analysis (supporting); investigation (supporting); methodology (supporting); validation (supporting); writing—review & editing (supporting). **Ondřej Zobač**: formal analysis (supporting); investigation (supporting); methodology (supporting); validation (supporting); writing—review & editing (supporting). **Melanie Todt**: funding acquisition (supporting); project administration (supporting); resources (supporting); supervision (supporting); validation (supporting); writing review & editing (supporting). **Daniel Koutný**: funding acquisition (lead); project administration (lead); resources (lead); supervision (lead); validation (lead); writing—review & editing (supporting).

## Acknowledgments

This publication was funded by the European Union under Horizon Europe Grant Agreement number 101079091 – BAANG. This publication was supported by the project “Mechanical Engineering of Biological and Bio-inspired Systems”, funded as project No. CZ.02.01.01/00/22\_008/0004634 by Programme Johannes Amos Comenius, call Excellent Research. The authors thank Vít Šreibr and Samuel Lukačovič for L-PBF production and acquiring the metallographic images.

Open access publishing facilitated by Vysoke uceni technicke v Brne, as part of the Wiley - CzechELib agreement.

## Funding

This publication was funded by the European Union under Horizon Europe Grant Agreement number 101079091 – BAANG. This publication was supported by the project “Mechanical Engineering of Biological and Bio-inspired Systems”, funded as project No. CZ.02.01.01/00/22\_008/0004634 by Programme Johannes Amos Comenius, call Excellent Research.

## Conflicts of Interest

The authors declare no conflicts of interest.

## Data Availability Statement

The data that support the findings of this study are openly available in the Zenodo repository at 10.5281/zenodo.14499514.

The original version of the authors' preprint of this study is openly available in the Zenodo Repository at 10.5281/zenodo.17182211.

## References

- H. Qian, H. Li, G. Song, and W. Guo, “A Constitutive Model for Superelastic Shape Memory Alloys considering the Influence of Strain Rate,” *Mathematical Problems in Engineering* 2013 (2013): 248671.
- L. Marandi, and I. Sen, “In-Vitro Mechanical Behavior and High Cycle Fatigue Characteristics of NiTi-Based Shape Memory Alloy Wire,” *International Journal of Fatigue* 148 (2021): 106226, <https://doi.org/10.1016/j.ijfatigue.2021.106226>.
- J. Mohd Jani, M. Leary, A. Subic, and M. A. Gibson, “A Review of Shape Memory Alloy Research, Applications and Opportunities,” *Materials and Design* 56 (2014): 1078–1113, <http://dx.doi.org/10.1016/j.matdes.2013.11.084>.
- F. Auricchio, R. L. Taylor, and J. Lubliner, “Shape-Memory Alloys: Macromodelling and Numerical Simulations of the Superelastic Behavior,” *Computer methods in applied mechanics and engineering* 146, 1997): 281.
- Z. Rao, X. Wang, J. Leng, Z. Yan, and X. Yan, “Design Methodology of the Ni50Ti50 Shape Memory Alloy Beam Actuator: Heat Treatment, Training and Numerical Simulation,” *Materials and Design* 217 (2022): 110615, <https://doi.org/10.1016/j.matdes.2022.110615>.

- R. A. Abubakar, F. Wang, and L. Wang, “A Review on Nitinol Shape Memory Alloy Heat Engines,” *Smart Materials and Structures* 30, no. 1 (2020): 013001.
- E. Farber, J. N. Zhu, A. Popovich, and V. Popovich, “A Review of NiTi Shape Memory Alloy as a Smart Material Produced by Additive Manufacturing,” *Materials Today: Proceedings* 30 (2019): 761–767, <https://doi.org/10.1016/j.matpr.2020.01.563>.
- Z. Yan, J.-N. Zhu, E. Borisov, T. Riemslog, S. P. Scott, M. Hermans, J. Jovanova, and V. Popovich, “Superelastic Response and Damping Behavior of Additively Manufactured Nitinol Architected Materials,” *Additive Manufacturing* 68 (2023): 103505.
- S. Kumar S, L. Marandi, V. K. Balla, S. Bysakh, D. Piorunek, G. Eggeler, M. Das, and I. Sen, “Microstructure – Property Correlations for Additively Manufactured NiTi Based Shape Memory Alloys,” *Materialia* 8 (2019): 100456, <https://doi.org/10.1016/j.mtla.2019.100456>.
- Z. Yu, Z. Xu, Y. Guo, R. Xin, R. Liu, C. Jiang, L. Li, Z. Zhang, and L. Ren, “Study on Properties of SLM-NiTi Shape Memory Alloy under the Same Energy Density,” *Journal of Materials Research and Technology* 13 (2021): 241–250, <https://doi.org/10.1016/j.jmrt.2021.04.058>.
- Q. Ren, C. Chen, Z. Lu, X. Wang, H. Lu, S. Yin, Y. Liu, H. Li, J. Wang, and Z. Ren, “Effect of a Constant Laser Energy Density on the Evolution of Microstructure and Mechanical Properties of NiTi Shape Memory Alloy Fabricated by Laser Powder Bed Fusion,” *Optics and Laser Technology* 152 (2022): 108182, <https://doi.org/10.1016/j.optlastec.2022.108182>.
- C. Zhang, L. Xue, S. A. Pestka, M. Ranaiefar, K. C. Atli, P. Honarmandi, R. Arróyave, I. Karaman, and A. Elwany, “Processing Parameters and Martensitic Phase Transformation Relationships in near Defect-Free Additively Manufactured NiTiHF High Temperature Shape Memory Alloys,” *Materials and Design* 222 (2022): 110988, <https://doi.org/10.1016/j.matdes.2022.110988>.
- J. C. Chekotu, R. Goodall, D. Kinahan, and D. Brabazon, “Control of Ni-Ti Phase Structure, Solid-State Transformation Temperatures and Enthalpies via Control of L-PBF Process Parameters,” *Materials and Design* 218 (2022): 110715, <https://doi.org/10.1016/j.matdes.2022.110715>.
- C. Tan, S. Li, K. Essa, P. Jamshidi, K. Zhou, W. Ma, and M. M. Attallah, “Laser Powder Bed Fusion of Ti-Rich TiNi Lattice Structures: Process Optimisation, Geometrical Integrity, and Phase Transformations,” *International Journal of Machine Tools and Manufacture* 141 (2019): 19–29, <https://doi.org/10.1016/j.ijmactools.2019.04.002>.
- A. Timercan, D. Campion, P. Terriault, and V. Brailovski, “Laser Powder Bed Fusion of Superelastic Ti-Ni Lattice Structures: Process Design and Testing,” *Journal of Manufacturing and Materials Processing* 8, no. 4 (2024): 176.
- J. Ge, B. Yuan, H. Chen, J. Pan, Q. Liu, M. Yan, Z. Lu, S. Zhang, and L. Zhang, “Anisotropy in Microstructural Features and Tensile Performance of Laser Powder Bed Fusion NiTi Alloys,” *Journal of Materials Research and Technology* 24 (2023): 8656–8668.
- E. McCumiskey, W. M. Dempster, D. H. Nash, T. R. Ashton, and D. G. Stevenson, “The Determination and Evaluation of Nitinol Constitutive Models for Finite Element Analysis,” *Applied Mechanics and Materials* 7–8 (2007): 81–88.
- S. Saedi, A. S. Turabi, M. Taheri Andani, C. Haberland, H. Karaca, and M. Elahinia, “The Influence of Heat Treatment on the Thermomechanical Response of Ni-Rich NiTi Alloys Manufactured by Selective Laser Melting,” *Journal of Alloys and Compounds* 677 (2016): 204–210, <http://dx.doi.org/10.1016/j.jallcom.2016.03.161>.
- E. Henderson, D. H. Nash, and W. M. Dempster, “On the Experimental Testing of Fine Nitinol Wires for Medical Devices,” *Journal of the Mechanical Behavior of Biomedical Materials* 4, no. 3 (2011): 261–268, <http://dx.doi.org/10.1016/j.jmbbm.2010.10.004>.
- W. Chen, D. Gu, J. Yang, Q. Yang, J. Chen, and X. Shen, “Compressive Mechanical Properties and Shape Memory Effect of

- NiTi Gradient Lattice Structures Fabricated by Laser Powder Bed Fusion,” *International Journal of Extreme Manufacturing* 4, no. 4 (2022): 045002.
21. S. Ehsan Saghalian, M. Nematollahi, G. Toker, A. Hinojos, N. Shayesteh Moghaddam, S. Saedi, C. Y. Lu, M. Javad Mahtabi, M. J. Mills, M. Elahinia, and H. E. Karaca, “Effect of Hatch Spacing and Laser Power on Microstructure, Texture, and Thermomechanical Properties of Laser Powder Bed Fusion (L-PBF) Additively Manufactured NiTi,” *Optics and Laser Technology* 149 (2022): 107680, <https://doi.org/10.1016/j.optlastec.2021.107680>.
22. T. R. K. Dora, R. Goud, A. Sahadevan, A. H. Chand, et al., Investigations into Sample Geometry Effects on the Superelastic and Fatigue Behavior of Nitinol: Modeling and Experiments, *Materialia* 20 (2021): 101256.
23. C. Zhang, J. Jin, M. He, and L. Yang, “Compressive Mechanics and Hyperelasticity of Ni-Ti Lattice Structures Fabricated by Selective Laser Melting,” *Crystals* 12, no. 3 (2022): 408.
24. V. P. Iasnii and R. Junga, “Phase Transformations and Mechanical Properties of the Nitinol Alloy with Shape Memory,” *Materials Science* 54, no. 3 (2018): 406–411.
25. Q. Yang, K. Sun, C. Yang, M. Sun, H. Peng, X. Shen, S. Huang, and J. Chen, “Compression and Superelasticity Behaviors of NiTi Porous Structures with Tiny Strut Fabricated by Selective Laser Melting,” *Journal of Alloys and Compounds* 858 (2021): 157674, <https://doi.org/10.1016/j.jallcom.2020.157674>.
26. T. Gustmann, F. Gutmann, F. Wenz, P. Koch, R. Stelzer, W.-G. Drossel, and H. Korn, “Properties of a Superelastic NiTi Shape Memory Alloy Using Laser Powder Bed Fusion and Adaptive Scanning Strategies,” *Progress in Additive Manufacturing* 5, no. 1 (2020): 11–18, <https://doi.org/10.1007/s40964-020-00118-6>.
27. G. Fangmin, Y. Guo, X. Kong, Z. Xiong, and S. Hao, “The Effect of Wall Thickness and Scanning Speed on the Martensitic Transformation and Tensile Properties of Selective Laser Melted NiTi Thin-Wall Structures,” *Metals* 12, no. 3 (2022): 519.
28. S. Dadbakhsh, B. Vrancken, J. P. Kruth, J. Luyten, and J. Van Humbeeck, “Texture and Anisotropy in Selective Laser Melting of NiTi Alloy,” *Materials Science and Engineering: A* 650 (2016): 225–232, <http://dx.doi.org/10.1016/j.msea.2015.10.032>.
29. M. Li, O. Contreras-Almengor, J. A. Ordoño, C. Aguilar Vega, R. Zapata Martínez, M. Echeverry-Rendón, A. Díaz-Lantada, and J. Molina-Aldareguia, “The Microstructure and Mechanical Properties of Nitinol Manufactured by LPBF: Differences between Ni-Rich and Ti-Rich Compositions,” *Virtual and Physical Prototyping* 20, no. 1 (2025): e2476006, <https://doi.org/10.1080/17452759.2025.2476006>.
30. Z. Xiang, Q. Yang, T. Zhang, X. Shen, J. Chen, and S. Huang, “Effect of Process Parameters on Superelasticity of LPBF Ni-Rich Ni51.3Ti48.7 Shape Memory Alloy,” *Metals* 14, no. 9 (2024): 961.
31. P. Jamshidi, C. Panwisawas, E. Langi, S. C. Cox, J. Feng, L. Zhao, and M. M. Attallah, “Development, Characterisation, and Modelling of Processability of Nitinol Stents Using Laser Powder Bed Fusion,” *Journal of Alloys and Compounds* 909 (2022): 164681, <https://doi.org/10.1016/j.jallcom.2022.164681>.
32. Z. Xiong, H. Li, H. Yang, Y. Yang, Y. Liu, L. Cui, X. Li, L. Masseling, L. Shen, and S. Hao, “Micro Laser Powder Bed Fusion of NiTi Alloys with Superior Mechanical Property and Shape Recovery Function,” *Additive Manufacturing* 57 (2022): 102960, <https://doi.org/10.1016/j.addma.2022.102960>.
33. T. Biasutti, P. Bettini, A. M. Grande, G. Sala, B. M. Colosimo, and A. Nespoli, “An in-Depth Study of a Thin-Wall Origami-Inspired NiTi Structure Fabricated through Laser Powder Bed Fusion,” *Progress in Additive Manufacturing* 10, no. 10 (2025): 7803–7814, <https://doi.org/10.1007/s40964-025-01073-w>.
34. R. Vrána, O. Červinek, P. Mañas, D. Koutný, and D. Paloušek, “Dynamic Loading of Lattice Structure Made by Selective Laser Melting-Numerical Model with Substitution of Geometrical Imperfections,” *Materials*. (2018)
35. J.-N. Zhu, E. Borisov, X. Liang, R. Huizenga, A. Popovich, V. Bliznuk, R. Petrov, M. Hermans, and V. Popovich, “Controlling Microstructure Evolution and Phase Transformation Behavior in Additive Manufacturing of Nitinol Shape Memory Alloys by Tuning Hatch Distance,” *Journal of Materials Science* 57, no. 10 (2022): 6066–6084, <https://doi.org/10.1007/s10853-022-07007-z>.
36. D. Bourke, K. T. Selvam, M. A. Obeidi, I. U. Ahad, and D. Brabazon, “Effect of Powder and Process Parameters on in-Situ Alloying of Nitinol during Laser Powder Bed Fusion,” *Journal of Materials Research and Technology* 30, no. May (2024): 7988–7997.
37. Q. Deng, X. Wang, Q. Lan, Z. Chang, Z. Liu, N. Su, Y. Wu, D. Liu, L. Peng, and W. Ding, “Limitations of Linear Energy Density for Laser Powder Bed Fusion of Mg-15Gd-1Zn-0.4Zr Alloy,” *Materials Characterization* 190 (2022): 112071, <https://doi.org/10.1016/j.matchar.2022.112071>.
38. P. U. Kelkar, H. S. Kim, K.-H. Cho, J. Y. Kwak, C.-Y. Kang, and H.-C. Song, “Cellular Auxetic Structures for Mechanical Metamaterials: A Review,” *Sensors* 20, no. 11 (2020): 3132.
39. H. M. A. Kolken and A. A. Zadpoor, “Auxetic Mechanical Metamaterials,” *RSC Advances* 7, no. 9 (2017): 5111–5129.
40. E. Vaglio, M. De, L. Thomas, et al., “Single Tracks Data Obtained by Selective Laser Melting of Ti6Al4V with a Small Laser Spot Diameter,” *Data in Brief* 33 (2020): 106443, <https://doi.org/10.1016/j.dib.2020.106443>.
41. S. Wei, J. Zhang, L. Zhang, Y. Zhang, B. Song, X. Wang, J. Fan, Q. Liu, and Y. Shi, “Laser Powder Bed Fusion Additive Manufacturing of NiTi Shape Memory Alloys: A Review,” *International Journal of Extreme Manufacturing* 5, no. 3 (2023): 032001.
42. X. Wang, J. Yu, J. Liu, L. Chen, Q. Yang, H. Wei, J. Sun, Z. Wang, Z. Zhang, G. Zhao, and J. Van Humbeeck, “Effect of Process Parameters on the Phase Transformation Behavior and Tensile Properties of NiTi Shape Memory Alloys Fabricated by Selective Laser Melting,” *Additive Manufacturing* 36 (2020): 101545, <http://dx.doi.org/10.1016/j.addma.2020.101545>.
43. Y. Yang, J. B. Zhan, Z. Z. Sun, H. L. Wang, et al., “Evolution of Functional Properties Realized by Increasing Laser Scanning Speed for the Selective Laser Melting Fabricated NiTi Alloy,” *Journal of Alloys and Compounds* 804 (2019): 220–229, <https://doi.org/10.1016/j.jallcom.2019.06.340>.
44. S. Saedi, N. Shayesteh Moghaddam, A. Amerinatanzi, M. Elahinia, and H. E. Karaca, “On the Effects of Selective Laser Melting Process Parameters on Microstructure and Thermomechanical Response of Ni-Rich NiTi,” *Acta Materialia* 144 (2018): 552–560, <http://dx.doi.org/10.1016/j.actamat.2017.10.072>.
45. J.-N. Zhu, Z. Ding, E. Borisov, X. Yao, J. C. Brouwer, A. Popovich, M. Hermans, and V. Popovich, “Healing Cracks in Additively Manufactured NiTi Shape Memory Alloys,” *Virtual and Physical Prototyping* 18, no. 1 (2023): e2246437.
46. N. Shayesteh Moghaddam, S. Saedi, A. Amerinatanzi, A. Hinojos, A. Ramazani, J. Kundin, M. J. Mills, H. Karaca, and M. Elahinia, “Achieving Superelasticity in Additively Manufactured NiTi in Compression without Post-Process Heat Treatment,” *Scientific Reports* 9, no. 1 (2019): 41, <http://dx.doi.org/10.1038/s41598-018-36641-4>.
47. T. Liu, Z. Wu, W. Zhou, M. Zhong, J. Lin, and Y. Yang, “Quasilinear Pseudoelasticity and Small Hysteresis in SLM-Fabricated NiTi,” *Journal of Alloys and Compounds* 933 (2023): 167694, <https://doi.org/10.1016/j.jallcom.2022.167694>.
48. M. Nematollahi, S. E. Saghalian, K. Safaei, P. Bayati, P. Bassani, C. Biffi, A. Tuissi, H. Karaca, and M. Elahinia, “Building Orientation-Structure-Property in Laser Powder Bed Fusion of NiTi Shape

- Memory Alloy,” *Journal of Alloys and Compounds* 873 (2021): 159791, <https://doi.org/10.1016/j.jallcom.2021.159791>.
49. X. Lu, G. Li, L. Liu, X. Zhu, and S.-T. Tu, “Effect of Ambient Temperature on Compressibility and Recovery of NiTi Shape Memory Alloys as Static Seals,” *Advances in Mechanical Engineering* 9, no. 2 (2017): 1687814017692287.
50. G. Li, T. Yu, N. Zhang, and M. Chen, “The Effect of Ni Content on Phase Transformation Behavior of NiTi Alloys: An Atomistic Modeling Study,” *Computational Materials Science* 215 (2022): 111804, <https://doi.org/10.1016/j.commatsci.2022.111804>.
51. K. Kus and T. Breczko, “DSC-Investigations of the Effect of Annealing Temperature on the Phase Transformation Behaviour in Ni-Ti Shape Memory Alloy,” *Materials Physics and Mechanics* 9, no. 1 (2010): 75–83.
52. J. Zhan, J. Wu, R. Ma, K. Li, J. Lin, and L. E. Murr, “Tuning the Functional Properties by Laser Powder Bed Fusion with Partitioned Repetitive Laser Scanning: Toward Editable 4D Printing of NiTi Alloys,” *Journal of Manufacturing Processes* 101 (2023): 1468–1481.
53. V. M. Dornelas, S. A. Oliveira, M. A. Savi, P. M. C. L. Pacheco, and L. F. G. de Souza, “Fatigue on Shape Memory Alloys: Experimental Observations and Constitutive Modeling,” *International Journal of Solids and Structures* 213 (2021): 1–24, <https://doi.org/10.1016/j.ijsolstr.2020.11.023>.
54. L. E. Murr, E. Martinez, K. N. Amato, S. M. Gaytan, J. Hernandez, D. A. Ramirez, P. W. Shindo, F. Medina, and R. B. Wicker, “Fabrication of Metal and Alloy Components by Additive Manufacturing: Examples of 3D Materials Science,” *Journal of Materials Research and Technology* 1, no. 1 (2012): 42–54, [http://dx.doi.org/10.1016/S2238-7854\(12\)70009-1](http://dx.doi.org/10.1016/S2238-7854(12)70009-1).
55. T. Ishimoto, K. Hagihara, K. Hisamoto, and T. Nakano, “Stability of Crystallographic Texture in Laser Powder Bed Fusion: Understanding the Competition of Crystal Growth Using a Single Crystalline Seed,” *Additive Manufacturing* 43 (2021): 102004, <https://doi.org/10.1016/j.addma.2021.102004>.
56. K. Safaei, N. T. Andani, B. Poorganji, M. T. Andani, and M. Elahinia, “Controlling Texture of NiTi Alloy Processed by Laser Powder Bed Fusion: Smart Build Orientation and Scanning Strategy,” *Additive Manufacturing Letters* 5 (2023): 100126, <https://doi.org/10.1016/j.addlet.2023.100126>.
57. T. Bormann, B. Müller, M. Schinhammer, A. Kessler, P. Thalmann, and M. de Wild, “Microstructure of Selective Laser Melted Nickel-Titanium,” *Materials Characterization* 94 (2014): 189–202.
58. J. F. Xiao, C. Cayron, M. Van der Meer, and R. E. Logé, “EBSD Study of Variant Reorientation, Texture, and Twin Formation in a Martensitic NiTi Alloy Deformed in Compression,” *Acta Materialia* 264 (2024): 119553.
59. J. F. Xiao, C. Cayron, and R. E. Logé, “An Investigation on Reorientation and Textural Evolution in a Martensitic NiTi Rolled Sheet Using EBSD,” *International Journal of Plasticity* 159 (2022): 103468.
60. O. Tyc, E. Iaparova, O. Molnárová, L. Heller, and P. Šittner, “Stress Induced Martensitic Transformation in NiTi at Elevated Temperatures: Martensite Variant Microstructures, Recoverable Strains and Plastic Strains,” *Acta Materialia* 279 (2024).
61. K. Gall, J. Tyber, G. Wilkesanders, S. W. Robertson, R. O. Ritchie, and H. J. Maier, “Effect of Microstructure on the Fatigue of Hot-Rolled and Cold-Drawn NiTi Shape Memory Alloys,” *Materials Science and Engineering: A* 486, no. 1-2 (2008): 389–403.
62. H. Kato, and K. Sasaki, “Transformation-Induced Plasticity as the Origin of Serrated Flow in an NiTi Shape Memory Alloy,” *International Journal of Plasticity* 50 (2013): 37–48, <http://dx.doi.org/10.1016/j.ijplas.2013.03.011>.
63. G. Eggeler, E. Hornbogen, A. Yawny, A. Heckmann, and M. Wagner, “Structural and Functional Fatigue of NiTi Shape Memory Alloys,” *Materials Science and Engineering: A* 378, no. 1-2 (2004): 24–33.
64. L. Orgéas and D. Favier, “Non-Symmetric Tension-Compression Behaviour of NiTi Alloy,” *Journal De Physique IV* 05, no. C8 (1995): C8-605– C8-610.
65. W.-N. Hsu, E. Polatidis, M. Šmíd, S. Van Petegem, N. Casati, and H. Van Swygenhoven, “Deformation and Degradation of Superelastic NiTi under Multiaxial Loading,” *Acta Materialia* 167 (2019): 149–158.
66. A. Bagheri, M. J. Mahtabi, and N. Shamsaei, “Fatigue Behavior and Cyclic Deformation of Additive Manufactured NiTi,” *Journal of Materials Processing Technology* 252 (2018): 440–453, <http://dx.doi.org/10.1016/j.jmatprotec.2017.10.006>.
67. H. Jiang, X. Wang, R. Xi, G. Li, H. Wei, J. Liu, B. Zhang, S. Kustov, K. Vanmeensel, J. Van Humbeeck, and G. Zhao, “Size Effect on the Microstructure, Phase Transformation Behavior, and Mechanical Properties of NiTi Shape Memory Alloys Fabricated by Laser Powder Bed Fusion,” *Journal of Materials Science and Technology* 157 (2023): 200–212, <https://doi.org/10.1016/j.jmst.2023.02.026>.
68. S. V. Chernyshikhin, I. A. Pelevin, F. Karimi, and I. V. Shishkovsky, “The Study on Resolution Factors of LPBF Technology for Manufacturing Superelastic NiTi Endodontic Files,” *Materials* 15, no. 19 (2022): 6556.
69. A. A. Martin, N. P. Caltá, S. A. Khairallah, J. Wang, P. J. Depond, A. Y. Fong, V. Thampy, G. M. Guss, A. M. Kiss, K. H. Stone, C. J. Tassone, J. Nelson Weker, M. F. Toney, T. van Buuren, and M. J. Matthews, “Dynamics of Pore Formation during Laser Powder Bed Fusion Additive Manufacturing,” *Nature Communications* 10, no. 1 (2019): 987, <http://dx.doi.org/10.1038/s41467-019-10009-2>.